A multiscale modeling study of loss processes in block-copolymer-based solar cell nanodevices

Sergii Donets, Anton Pershin, Martin J. A. Christlmaier, and Stephan A. Baeurle

---

Articles you may be interested in

Optimizing the fabrication process and interplay of device components of polymer solar cells using a field-based multiscale solar-cell algorithm
J. Chem. Phys. 142, 184902 (2015); 10.1063/1.4919649

An analytical model for analyzing the current-voltage characteristics of bulk heterojunction organic solar cells
J. Appl. Phys. 115, 034504 (2014); 10.1063/1.4861725

Exciton annihilation as bimolecular loss in organic solar cells
J. Appl. Phys. 114, 154514 (2013); 10.1063/1.4825048

A new multiscale modeling method for simulating the loss processes in polymer solar cell nanodevices
J. Chem. Phys. 136, 194102 (2012); 10.1063/1.4712622

Efficient organic solar cells based on a double p - i - n architecture using doped wide-gap transport layers
Appl. Phys. Lett. 86, 244102 (2005); 10.1063/1.1935771

A multiscale modeling study of loss processes in block-copolymer-based solar cell nanodevices

Sergii Donets, Anton Pershin, Martin J. A. Christlmaier, and Stephan A. Baeurle[a]
Department of Chemistry and Pharmacy, Institute of Physical and Theoretical Chemistry,
University of Regensburg, D-93040 Regensburg, Germany

Flexible photovoltaic devices possess promising perspectives in opto-electronic technologies, where high mobility and/or large-scale applicability are important. However, their usefulness in such applications is currently still limited due to the low level of optimization of their performance and durability. For the improvement of these properties, a better understanding and control of small-scale annihilation phenomena involved in the photovoltaic process, such as exciton loss and charge carrier loss, is necessary, which typically implicates multiple length- and time-scales. Here, we study the causes for their occurrence on the example of nanostructured diblock- and triblock-copolymer systems by making use of a novel solar-cell simulation algorithm and explore new routes to optimize their photovoltaic properties. A particular focus is set on the investigation of exciton and charge carrier loss phenomena and their dependence on the inter-monomeric interaction strength, chain architecture, and external mechanical loading. Our simulation results reveal that in the regime from low up to intermediate χ-parameters an increasing number of continuous percolation paths is created. In this parameter range, the internal quantum efficiency (IQE) increases up to a maximum, characterized by a minimum in the number of charge losses due to charge recombination. In the regime of high χ-parameters both block-copolymer systems form nanostructures with a large number of bottlenecks and dead ends. These lead to a large number of charge losses due to charge recombination, charge trapping, and a deteriorated exciton dissociation, resulting in a significant drop in the IQE. Moreover, we find that the photovoltaic performance of the triblock-copolymer material decreases with increasing mechanical loading, caused by a growing number of charge losses due to charge recombination and charge accumulation. Finally, we demonstrate that the process of charge trapping in defects can be reversed by changing the polarity of the electrodes, which confers these materials the ability to be used as charge storage media. © *2013 American Institute of Physics.* [http://dx.doi.org/10.1063/1.4792366]

I. INTRODUCTION

Polymer solar cells are a promising new type of photovoltaic device with great potential in large area electronics, due to their easy manufacturing, high flexibility, light weight, and low production costs.[1,2] However, despite the significant progress in their synthesis and experimental characterization, their photoelectric power conversion efficiency is still rather small compared to their inorganic counterparts with maximum values reaching around 9%.[1,3] This has mainly been attributed to small-scale loss phenomena of the elementary particles occurring in the photovoltaic process, such as photon loss, exciton loss, and charge carrier loss.[4,5] These loss processes typically emerge at characteristic stages of the photovoltaic process, such as photon absorption, exciton generation and diffusion to the donor-acceptor (DA) heterojunction, exciton separation, and charge carrier generation at the DA heterojunction, diffusion of the charge carriers to the respective electrodes and/or collection of the charge carriers at the electrodes.[5,6] Exciton loss,[7] for instance, can take place through radiative recombination of an exciton via a first-

order decay reaction, giving rise to photoluminescence. This loss mechanism has been studied particularly extensively in thin polymer films through time-resolved photoluminescence measurements.[8] Another type of first-order decomposition reaction is the defect-mediated non-radiative exciton decay, providing a phonon. This phenomenon has been investigated, e.g., by Cordella *et al.*,[9] who used transient pump-probe spectroscopy to explore the interaction dynamics between excitons and intramolecular vibrations in α-sexithiophene crystals. An example for an exciton-loss mechanism through a second-order reaction is the process of exciton-exciton annihilation, where upon the collision of two excitons one is annihilated, whereas the other used the energy from the collision to be promoted to a higher energy level.[7] Such investigations have been carried out, e.g., by Martini *et al.*[10] and Lewis *et al.*,[11] who studied exciton-exciton annihilation in polymer films using time-resolved photoluminescence spectroscopy. Another type of small-scale annihilation phenomena, reducing the power conversion efficiency of polymer solar cells, are related to charge carrier losses. These can, e.g., be caused by the process of charge recombination,[12] which has been studied through a broad variety of experimental methods, such as time-of-flight (TOF),[13] steady-state current-voltage,[14,15]

---

[a]Electronic mail: stephan.baeurle@chemie.uni-regensburg.de.

impedance spectroscopy[16] as well as transient absorption and transient photovoltage measurements.[17] It has been found that at applied voltages above the maximum power point and at the open-circuit condition, bimolecular recombination reduces the current density and limits the fill factor, thereby decreasing the power conversion efficiency.[12] Another important kind of charge-loss process is known as charge trapping, in which charges are caught in a defect of the chain conformation or mesoscale morphology and may affect the free charges in close proximity. This leads to a lower charge carrier mobility and ultimately to a lower device performance. Such a phenomenon has been investigated, e.g., by time-resolved electrostatic force microscopy and scanning Kelvin probe imaging by Reid *et al.*[18] Due to the complex relationship of these loss mechanisms within the photovoltaic process and their strong dependence on the structural-dynamical characteristics of the material, their impact on the photovoltaic properties has not been minimized in a satisfactory way for the polymer solar-cell materials currently available.[5, 19] Therefore, it is not surprising that their power conversion efficiency is still relatively low, compared to their inorganic counterparts. For a simultaneous optimization of the photovoltaic steps previously mentioned, the generation of a clearly defined morphology with optimized film as well as phase thickness is of crucial importance, since it ensures that the electrons and holes can be separated and transported to the electrodes without losses.[20, 21] In particular, it has recently been established empirically that the generation of stable nanostructured bulk heterojunctions (BHJs), possessing continuous percolation paths for the charge carriers, as well as nanophases, having twice the size of the exciton diffusion length, is a major prerequisite for the increase of the performance of polymer solar cells. To optimize the photovoltaic process of these systems, one has, thus, to find an ideal compromise for the morphology as a function of the topology and chemical composition of the polymers, involved in the photovoltaic process, at various external conditions imposed on the system. Despite the undeniable progress of the experimental tools in elucidating the causes deteriorating the photovoltaic performance of polymer solar cells, it is still rather cost-intensive and time-consuming to perform extensive analyses of loss processes on a molecular or mesoscopic scale for polymer systems with changing chemical characteristics, such as different molecular constitution of the monomers, chemical composition, and/or chain architecture, solvents, and subjected to various external influences, such as temperature changes and/or mechanical loadings. Further difficulties in the investigation of these processes on the local scale can relate to the poor resolution and sensitivity of conventional experimental measurement tools, which often do not provide reliable information about complex polymer systems on various length- and time-scales. In this regard computer simulation techniques can provide to material scientists a powerful alternative to gain a deeper understanding of the physics and chemistry of polymer solar cell nanodevices.

One of the bottlenecks of most simulation tools in nanodevice applications is the computation of the structural-dynamical evolution of the interacting polymers, which is either inaccurate or too computationally demanding for the treatment of the multiscale problem under consideration.[22, 23]

To describe the structural-dynamics of complex polymer systems on different scales within the particle description, several computational methodologies have been developed starting from the late 1970s.[24] A prominent example among those is the molecular dynamics (MD) technique, which describes the time-evolution of many-particle systems through phase space by numerically integrating Newton's equations of motion.[25] However, since its range of applicability for small polymer systems with up to 10^5 atoms usually spans from nanoseconds up to sub-microseconds in diluted polymer solutions, its usefulness to study the structural rearrangement of the chains in pure polymer-melt or dense polymer-solvent systems on typical experimental timescales is only limited, due to lengthy equilibration times.[26, 27] In order to reach longer timescales with the MD technique, several approaches have been proposed in the past decades. One of those is the coarse-graining (CG) approach, in which the system's degrees of freedom and, thus, the number of interactions are reduced enabling the use of larger timesteps at lower computational costs. A successful CG method for polymer systems is the united-atom approach, implemented, e.g., in the optimized potentials for liquid simulations (OPLS) forcefield in its united-atom version (OPLS-ua).[28] It consists in representing all hydrogens with their respective aliphatic carbons as single effective atomic units. More severe and systematic coarse-graining approaches, such as the iterative Boltzmann inversion, force-matching, and inverse Monte Carlo techniques implemented, e.g., in the VOTCA package,[29] reliably reproduce structures of simple polymers. But they generally fail in reproducing the correct structural-dynamical evolution of more sophisticated polymer systems, due to their slow relaxation times and strong heterogeneity at the atomistic level of description. Other methods based on a continuum description of the underlying polymer model permit to obtain qualitative estimates of the physical properties of polymer systems, subjected to small external changes in the linear regime.[30] However, they fail in providing reliable predictions of complex structural-dynamical characteristics. To cope with the structural-dynamical evolution of large-scale polymer systems with up to several million of atoms,[22] methods based on the field-theoretic formalism have been devised in the past two decades, which rely on the concept of transforming the many-body partition function integral from the conventional particle representation to an alternative field-functional-integral representation. The conversion can be achieved with the so-called Hubbard-Stratonovich transformation,[31] which enables the substitution of the original particle degrees of freedom with scalar field degrees of freedom. A major advantage of field-theoretic approaches results from their favorable approximation characteristics of the corresponding functional integrals, which allow the development of reliable approximation strategies for the cost-efficient treatment of large sophisticated polymer systems. One effective and widely used approximation procedure is, for instance, the so-called mean-field (MF) approximation.[22] Its basic idea consists in decoupling the many-body interaction term of the potential energy in the partition function integral and replace it with an action functional, which describes the interaction of independent particles (monomers) with an average mean field. This procedure reduces in a suitable way the many-particle

problem in an effective one-particle problem and provides a reliable approximation, under the assumption that the partition function integral of the system is mainly dominated by the MF configuration. A major benefit from solving the many-particle problem within the MF approximation or with its numerical implementation the so-called self-consistent-field theory (SCFT) method, which will be introduced in the following, is that it provides in many otherwise intractable situations reliable information about the structure and physical properties of complex many-particle systems at relatively low computational costs. The SCFT method has been proven useful for generating morphologies of soft polymer systems with arbitrary chain architecture, such as linear polymers, branched polymers with arbitrary topology, copolymers with different monomeric sequences (block, random, or tapered) in melts or solutions.[22,32,33] Methods going beyond the MF level have been introduced recently and may be used for computing the structural-dynamical characteristics of polymer-solvent systems with strong repulsive interactions between monomers, which may arise, e.g., in cases where the polymers possess polar or ionic groups in the semi-dilute or dilute concentration regime.[22,33–36] In a recent work,[5] we have extended the range of application of the field-theoretic methods mentioned previously, to investigate the loss processes of charge carriers and excitons in defect structures of nanostructured polymer solar cells. This approach is based on combining either the time-dependent Ginzburg-Landau method or the SCFT method, to generate morphologies of different scale of phase separation and degree of defect formation, with a first reaction (FR)-type dynamic Monte Carlo (DMC) method, to simulate the elementary photovoltaic processes involving the charge carriers and excitons within a particle description. From these investigations, we deduced that structural inhomogeneities, such as bottlenecks and dead ends, significantly affect the internal quantum efficiency of the nanostructured polymer solar cells. Moreover, we concluded that loss phenomena, caused by charge recombination and charge accumulation, lead to a dramatic decrease in their internal quantum efficiency and that, consequently, the impact of these processes must be reduced to improve the photovoltaic performance of these materials.

In the present work, we study the causes affecting the loss processes of elementary particles involved in the photovoltaic process of polymer solar cells with changing chemical characteristics and external conditions, imposed on the system. To this end, we apply the multiscale DMC-SCFT algorithm mentioned previously on systems composed of DA-diblock- and ADA-triblock-copolymers and compare their photovoltaic performance as a function of the interaction strength between the monomers, chain architecture as well as external mechanical loadings. Finally, we investigate the suitability of these polymer systems for the purpose of charge storage by analyzing their charge storage capacity as well as charge loading/unloading behavior.

Our paper is organized in the following way. In Sec. II, we provide a short review of the DMC-SCFT algorithm and introduce the model parameters used in our solar-cell simulations. Afterwards, in Sec. III we present and discuss the simulation results, obtained from the application of our algorithm on the block-copolymer systems mentioned previously. Finally, we end our paper with a summary and a brief outlook.

II. METHODS AND SIMULATION DETAILS

To compute the photovoltaic properties of the block-copolymer systems considered in this paper, we make use of our recently developed multiscale solar cell algorithm, which relies on the coupling of a mesoscopic field-theoretic approach, to generate the nanoscale morphology of the polymer system under consideration, with a suitable DMC algorithm, to model the elementary photovoltaic processes.[5] To keep the problem computationally tractable, we determine the equilibrium morphologies of the block-copolymer systems by approximating the corresponding polymer-field theories at the MF level. An efficient numerical strategy, relying on this approximation, is the SCFT method.[37–39] In the following, we briefly review the SCFT method for a melt composed of AB-diblock copolymers,[39] for which, due to screening effects between the monomers, we can assume Gaussian statistics for the chain conformation. Within this approximation, each polymer chain consists of N_A segments of A-type and N_B segments of B-type with their respective statistical segment lengths b_A and b_B, which means that the total number of statistical segments of a chain is $N = N_A + N_B$. To distinguish each segment, we consider that the configuration of the αth chain can be described by a space curve $\mathbf{r}_\alpha(s)$ parameterized by the chain contour variable s, where the ranges $0 \leq s \leq N_A$ and $N_A \leq s \leq N$ describe, respectively, the A-block and B-block with $s = 0$ as the free end of the A-block and $s = N$ as the other free end of the B-block. Let us next define the partition function integral $Q(s', \mathbf{r}'; s, \mathbf{r})$, representing the equilibrium statistical weight of a subchain between the sth- and s'th-segment with $(0 \leq s' \leq s \leq N)$ that is fixed at the positions $\mathbf{r}$ and $\mathbf{r}'$. This statistical weight can be evaluated within the MF approximation by solving the following Schrödinger-type evolution equation:

$$\frac{\delta}{\delta s} Q(s', \mathbf{r}'; s, \mathbf{r})$$
$$= \begin{cases} \left[\frac{b_A^2}{6} \nabla^2 - \beta V_A(\mathbf{r}) \right] Q(s', \mathbf{r}'; s, \mathbf{r}), & 0 \leq s \leq N_A, \\ \left[\frac{b_B^2}{6} \nabla^2 - \beta V_B(\mathbf{r}) \right] Q(s', \mathbf{r}'; s, \mathbf{r}), & N_A \leq s \leq N, \end{cases}$$

$$(1)$$

where $\beta = 1/(k_B T)$ and $V_A(\mathbf{r})$ as well as $V_B(\mathbf{r})$ are external potentials, acting on A- or B-type segments at position $\mathbf{r}$. The latter functions represent MF potentials, resulting from the interaction between the segments as well as from enforcing the incompressibility condition, and are obtained in a self-consistent fashion. Moreover, the initial condition for Eq. (1) is given by $Q(0, \mathbf{r}'; 0, \mathbf{r}) = \delta(\mathbf{r} - \mathbf{r}')$. Because the two ends of the block copolymer are not equivalent, we need to introduce an additional statistical weight $Q^\dagger(s', \mathbf{r}'; s, \mathbf{r})$, which is calculated in the opposite direction along the chain starting from the free end $s = N$. To reduce the computational expense, we

define in the following the integrated statistical weights:

$$q(s, \mathbf{r}) = \int d\mathbf{r}' \, Q(0, \mathbf{r}'; s, \mathbf{r}),$$

$$q^\dagger(s, \mathbf{r}) = \int d\mathbf{r}' \, Q^\dagger(0, \mathbf{r}'; s, \mathbf{r}). \tag{2}$$

These latter weights can be proven to satisfy Eq. (1) similarly as the non-integrated ones. This then leads to the following diffusion equation:

$$\frac{\delta}{\delta s} q(s, \mathbf{r}) = \begin{cases} \left[\frac{b_A^2}{6} \nabla^2 - \beta V_A(\mathbf{r}) \right] q(s, \mathbf{r}), & 0 \leq s \leq N_A, \\ \left[\frac{b_B^2}{6} \nabla^2 - \beta V_B(\mathbf{r}) \right] q(s, \mathbf{r}), & N_A \leq s \leq N \end{cases} \tag{3}$$

with the initial condition

$$q(0, \mathbf{r}) = 1. \tag{4}$$

Analogous expressions as in Eqs. (3) and (4) can be formulated for $q^\dagger(s, \mathbf{r})$. By using the definitions in Eqs. (2), the volume fractions of the A- and B-type segments at position $\mathbf{r}$ can be written as

$$\phi_A(\mathbf{r}) = C \int_0^{N_A} ds \, q(s, \mathbf{r}) q^\dagger(N - s, \mathbf{r}), \tag{5}$$

$$\phi_B(\mathbf{r}) = C \int_{N_A}^{N} ds \, q(s, \mathbf{r}) q^\dagger(N - s, \mathbf{r}), \tag{6}$$

where the normalization constant

$$C = \frac{V}{\int d\mathbf{r} \int ds \, q(s, \mathbf{r}) q^\dagger(N - s, \mathbf{r})} = \frac{V}{NZ} \tag{7}$$

with V as the total volume of the system and Z as the single-chain partition function. The external potential $V_K(\mathbf{r})$ of a K-type segment (K = A or B) can be decomposed into two terms in the following way:

$$V_K(\mathbf{r}) = \sum_{K'} \epsilon_{KK'} \phi_{K'}(\mathbf{r}) - \mu_K(\mathbf{r}), \tag{8}$$

where the first term represents the interaction energy between the segments with $\epsilon_{KK'}$ as the nearest-neighbor pair-interaction energy between a K-type and K'-type segment. The latter quantity is related to the Flory-Huggins interaction parameter through the following expression $\chi_{AB} = N_{ns}\beta[\varepsilon_{AB} - (1/2)(\varepsilon_{AA} + \varepsilon_{BB})]$, where N_{ns} is the number of nearest-neighbor sites. Moreover, the function $\mu_K(\mathbf{r})$ is the chemical potential of the K-type segment, which represents a Lagrange multiplier that enforces a constraint imposed on the system, such as the incompressibility condition. To obtain the volume fractions of the equilibrium nanostructured morphologies, the previous system of equations has to be solved in an iterative manner. First of all, the potential fields $V_A(\mathbf{r})$ and $V_B(\mathbf{r})$ are determined from the volume fractions $\phi_A(\mathbf{r})$ and $\phi_B(\mathbf{r})$ by making use of Eq. (8). Afterwards, the weights $q(s, \mathbf{r})$ and $q^\dagger(s, \mathbf{r})$ are calculated by solving Eqs. (3) and (4) that contain the fields $V_A(\mathbf{r})$ and $V_B(\mathbf{r})$. Finally, the new volume fractions $\phi_A(\mathbf{r})$ and $\phi_B(\mathbf{r})$ are calculated from the weights $q(s, \mathbf{r})$ and $q^\dagger(s, \mathbf{r})$ through Eqs. (5) and (6). The procedure is repeated until a self-consistent solution is reached. In our calculations,

we considered systems composed of symmetric AB-diblock copolymers with polymerization indices $N_A = N_B = 20$ and of symmetric ABA-triblock copolymers with polymerization indices $N_A = 10$ and $N_B = 20$. In both cases, we chose the statistical segment lengths as $b_A = b_B = b$. Moreover, we took a discrete lattice of size 64×64 with a spatial mesh width of Δ x = Δ y = 1 in units of b. For the numerical integration of the differential equation (3), we used a contour step size of $\Delta s = 1.0$ and computed the free energies with a relative accuracy of 10^{-4}. For a detailed derivation of the SCFT method and description of its implementation, we refer to Refs. 32 and 40, respectively. To compute the morphologies, we made use of the program package OCTA[41, 42] and performed the solar-cell simulations with our DMC algorithm for each of the morphologies, as described in the following.

To simulate the photovoltaic process,[5] we assumed that three types of elementary particles are present in the polymer solar cell device, i.e., electrons, holes, and excitons. Depending on the nature and environment of the elementary particles, they can exhibit the following algorithmic steps: (1) exciton generation by light absorption; (2) exciton motion within the material through diffusion or exciton annihilation; (3) exciton dissociation at the DA heterojunction with creation of an electron and a hole; (4) charge recombination or charge motion under the influence of the built-in electric field resulting from the difference between the electrode work functions; (5) charge collection at the appropriate electrodes. In our simulation study, we considered systems composed of DA-diblock copolymers and ADA-triblock copolymers, where the A- and D-blocks consisted of (R1,R2)-substituted poly(perylene diimide-alt-dithienothiophene) ((R1,R2)-PPDI-DTT) and (R1,R3)-substituted bis(thienylenevinylene)-substituted polythiophene ((R1,R3)-biTV-PT), respectively. In Fig. 1, we visualize the corresponding chemical structures of the A- and D-type monomers. We point out that the substituents are not connected to the π-system of the monomer cores and, thus, they do not affect the electronic structure of the polymers, which determines the parameters of the solar cell algorithm. We will vary them in the following to change the effective interactions and, thus, the χ-parameter between the monomers without modifying the parameters of the solar cell algorithm. In the calculations, we set the system temperature to T = 298 K and used a lattice size of 64×64 sites in conjunction with a lattice constant of $a_0 = 1$ nm. At each lattice site, we imposed a single occupancy constrain for the elementary particles and assumed that the majority component determines whether the site is either part of the electron-conducting or hole-conducting phase. To accomplish the dynamical evolution of the elementary particles, we used the FR method,[43, 44] which implies that all possible events are stored in a queue in order of ascending waiting times and that the event with the smallest waiting time is executed at first. Moreover, we assumed that the particle motion within the system occurs through hopping between different lattice sites. These hopping processes together with the other available processes, given in the summary of algorithmic steps listed previously, constituted the sequence of configurational changes that can take place during the system's evolution through phase space.
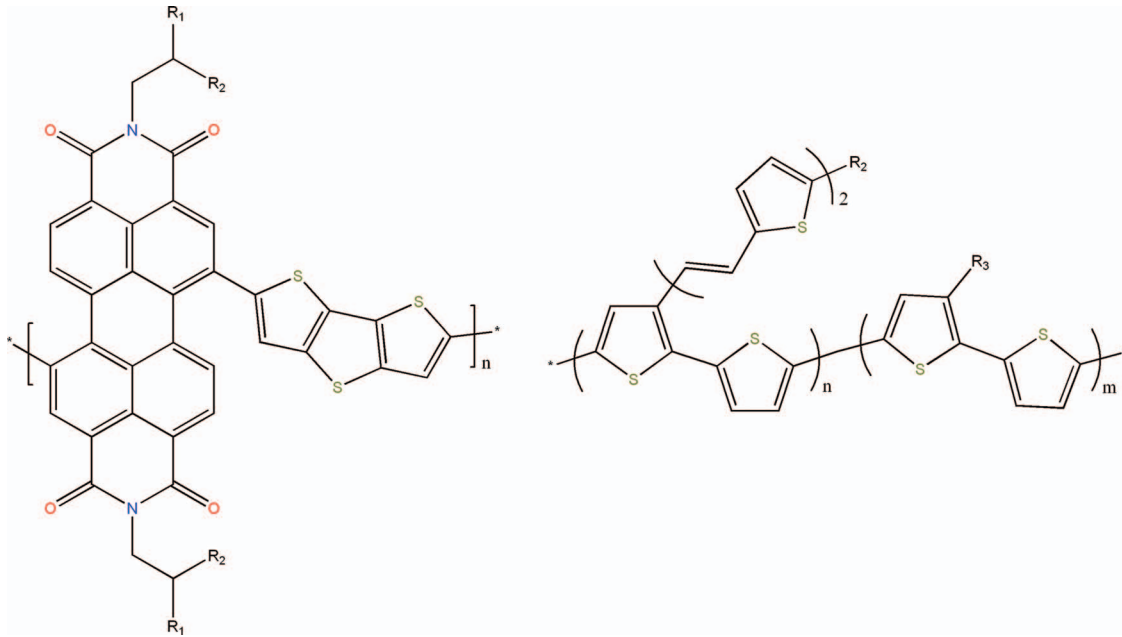
FIG. 1. Chemical structures of the A- and D-type monomers composed of blocks of (a) (R1,R2)-substituted poly(perylene diimide-alt-dithienothiophene) and (b) (R1,R3)-substituted bis(thienylenevinylene)-substituted poly-thiophene.[5,44]

The excitons were created at randomly chosen sites in the lattice with a constant rate of $\omega_{cre} = 900$ s^{-1} nm^{-2}, which has been determined from the AM1.5 solar spectrum with an illumination of 90 mW/cm^2 and the absorption spectrum of the polymer material.[44,45] The exciton hopping rate from lattice site i to a nearby site j has been calculated through[44]

$$\omega_{ij} = \omega_e \left(\frac{r_0}{r_{ij}} \right)^6 , \qquad (9)$$

where r_{ij} denotes the distance between the hopping sites i and j, whereas r_0 is the exciton-localization radius and ω_e is the hopping-attempt frequency. Note that the excitons on the lattice were allowed to jump within a radius of 6 nm in either the hole- or electron-conducting phase. The prefactor $\omega_e r_0^6 = 2$ nm^6 ps^{-1} as well as exciton recombination rate $\omega_{dec} = 0.002$ ps^{-1} were selected, to reproduce the experimental values of exciton diffusion length ($\sim$10 nm) and lifetime ($\sim$500 ps). The rate of hopping of charge carriers between nearest-neighbor lattice sites was calculated using the formula from the Marcus theory[46,47]

$$\omega_{ij} = V_{hop} \exp \left[-\frac{(\Delta E_{ij} + \lambda)^2}{4\lambda k_B T} \right], \qquad (10)$$

where

$$\Delta E_{ij} = E_j - E_i = \Delta E_{ij}^C + \Delta E_{ij}^I + \Delta E_{ij}^F + \Delta E_{ij}^\sigma \quad (11)$$

denotes the difference between the energies of hopping sites j and i, whereas k_B is Boltzmann's constant and $\lambda = 0.187$ eV is the reorganization energy corresponding to twice the polaronic binding energy.[48] In the previous equation, ΔE_{ij}^C represents the energy difference between the Coulombic interaction energies of the charges at site j and i with all other charges within a cutoff,[49] i.e.,

$$\Delta E_{ij}^C = E_j^C - E_i^C \qquad (12)$$

with

$$E_i^C = \sum_{j=1}^n \frac{qe}{4\pi \varepsilon_0 \varepsilon_r r_{ij}}, \qquad (13)$$

where n is the total number of other charges in the system within the cutoff r_c and e is the elementary charge with $q = +e$ for electron-electron and hole-hole repulsion as well as $q = -e$ for electron-hole attraction. The parameters $\varepsilon_0 \varepsilon_r$ designate the dielectric constant with ε_0 as the vacuum permittivity and $\varepsilon_r = 3.5$ the relative permittivity. We treated the long-range tail of the electrostatic contribution by cutting the Coulomb potential at $r_c = 10$ nm and shifting the function to zero as well as using periodic boundary conditions, applied in direction of the electrodes. The contribution of the polarization of the electrodes (image charge effect) was included through[49]

$$\Delta E_{ij}^I = \frac{e^2}{16\pi \varepsilon_0 \varepsilon_r} \left(\frac{1}{x_i} - \frac{1}{x_j} \right), \qquad (14)$$

where x_i and x_j denote the distances from the respective electrodes. Moreover, the energy contribution related to the action of the external and internal electrical fields on the charges was taken into account as follows:

$$\Delta E_{ij}^F = e \left[\mathcal{E}_{ext} - \mathcal{E}_{int} \right] (x_i - x_j), \qquad (15)$$

where $\mathcal{E}_{ext} = 0$ Vm^{-1} represents the external electrical field. The internal electrical field, which is caused by the built-in voltage resulting from the difference in work functions of the electrodes $\Delta \phi_w = 0.5$ V, was included through $\mathcal{E}_{int} = \Delta \phi_w / d$, where d defines the distance between the electrodes. In addition, to take into account the effect of energetic disorder of the material on the charges, we added the following contribution:

$$\Delta E_{ij}^\sigma = E_j^\sigma - E_i^\sigma , \qquad (16)$$

where E_i^σ is the energy from the Gaussian density-of-states (DOS) distribution and $\sigma = 0.062$ eV the corresponding standard deviation. The prefactor V_{hop} was obtained from the Einstein relationship for an isoenergetic material,[46,50,51] which is given by

$$V_{hop} = \frac{6k_B T \mu_{e/h}}{ea_0^2} \exp\left[\frac{\lambda}{4k_B T}\right], \qquad (17)$$

where $\mu_{e/h}$ defines the mobility of the electrons/holes in both polymer species and is taken as $\mu_{e/h} = 10^{-3}$ cm^2 V^{-1} s^{-1}. Note that in our simulations we assumed the electrons and holes to have equal mobilities and, hence, for both charge carrier types we chose $V_{hop} = 1.06 \times 10^{-2}$ ps^{-1}. In addition, we ensured that, if an electron and a hole are located on adjacent sites, they can recombine with the rate $\omega_{rec} = 10^{-6}$ ps^{-1}. To exclude the influence of the charge injections on the loss processes, we assumed that no charge injections take place at the electrodes.[44] All the simulations of the diblock-copolymer morphologies (I−IX) were run up to 50 000 generated excitons, whereas the simulations of the triblock-copolymer morphologies (I and III−VIII) as well as (II and IX) were run up to 100 000 and 75 000 generated excitons, respectively. Moreover, we considered the system to be equilibrated, when the deviations in the values of the exciton dissociation efficiency, charge transport efficiency and exciton lifetime did not exceed the preset error of 0.01% within a certain timespan in the production phase of the simulation. Finally, we generated the strained morphologies with the software tool MUFFIN/ELASTICA,[30,52] which is part of the OCTA-program package and is a multiphase linear elasticity simulator based on the finite-element method. For the straining, we used the morphology VI of the triblock-copolymer system, which is the morphology with the largest IQE of all triblock-copolymer morphologies over the entire χ-parameter range.

III. RESULTS AND DISCUSSION

We begin with the analysis of our simulation results by investigating the dependence of the photovoltaic properties of the polymer systems under consideration on the structural characteristics through varying their chemical composition and chain architecture. In Fig. 2, we visualize the morphologies, calculated with the static SCFT method, for a system of phase-separated (a) DA-diblock copolymers with block lengths 20A20D as well as (b) ADA-triblock copolymers with block lengths 10A20D10A as a function of the Flory-Huggins interaction parameter χ. From both graphs, we deduce that in the range from low up to intermediate χ-parameters the morphologies acquire an increasing degree of phase separation with decreasing interfacial length and change successively from unordered to lamellar-like structure. In case of the diblock-copolymer system, we see that for the morphology IV a maximum number of continuous percolation paths are formed, which are solely interrupted by a small number of dead ends. Moreover, we note that, starting from morphology IV up to morphology IX, the phases become again more fragmented by retaining a constant phase thickness, resulting in the creation of a growing number of dead ends and isolated inclusions. By contrast, in case of the triblock-copolymer sys-
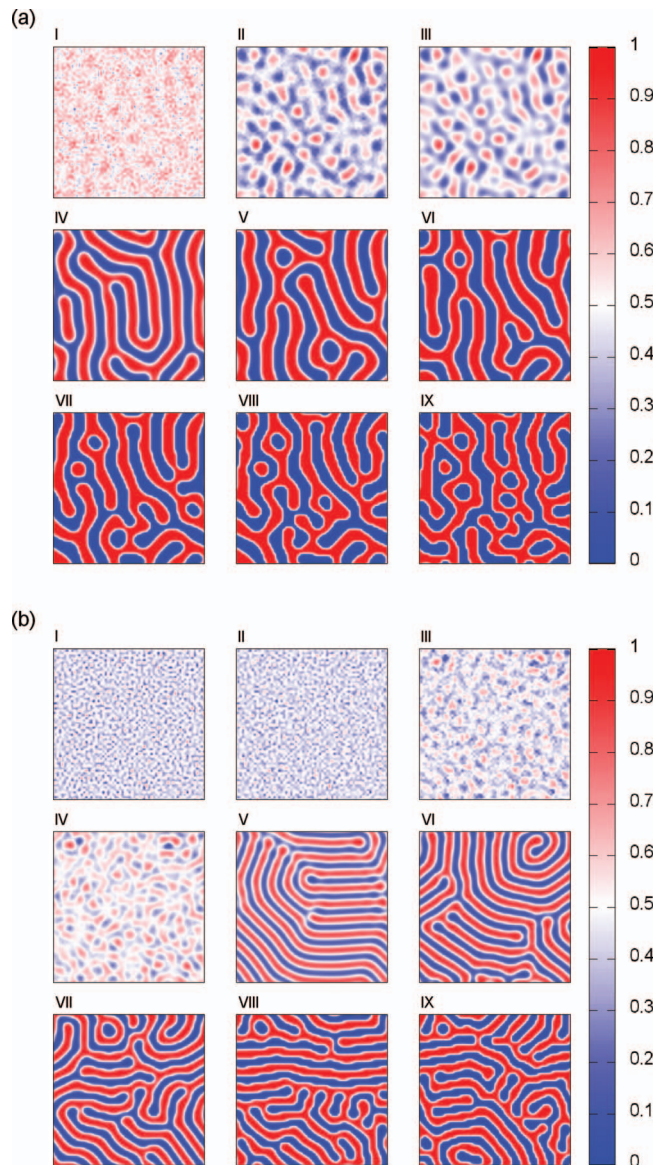

FIG. 2. Volume fractions for a system composed of (a) D20A20-diblock copolymers or (b) A10D20A10-triblock copolymers as a function of the Flory-Huggins interaction parameter, obtained with the static SCFT method [red: majority A phase (electron-conducting); blue: majority D phase (hole-conducting)].

tem we observe that continuous percolation paths are formed in the range from morphology V up to morphology IX with a maximum number of paths, obtained for the morphologies V and VI. Similarly, as in case of the diblock-copolymer system, the number of defects increases and transforms from dead ends to isolated inclusions, which lead to severely disconnected phases starting from morphology VII up to morphology IX. By further comparing these morphologies to the ones of the diblock copolymers, we conclude that the phases in case of the triblock copolymers are thinner and the nanostructures possess a larger interfacial length with a high degree of phase separation in the range from morphologies V up to IX. Next, in Fig. 3 we show the results for the internal quantum efficiency IQE, exciton dissociation efficiency (EDE), charge transport efficiency (CTE) for the systems composed of the phase-separated (a) DA-diblock copolymers as well as (b)
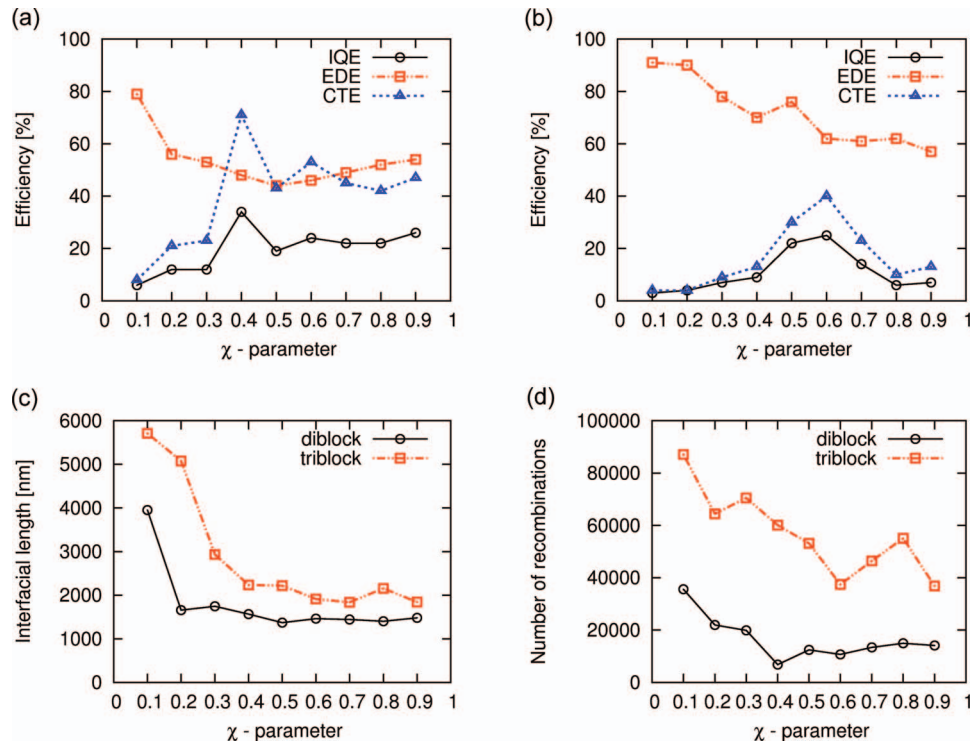
FIG. 3. Internal quantum efficiency (black), exciton dissociation efficiency (orange), charge transport efficiency (blue) for a system composed of (a) D20A20-diblock copolymers or (b) A10D20A10-triblock copolymers as a function of the Flory-Huggins interaction parameter, obtained with the DMC-SCFT method. Interfacial length (c) and total number of recombinations (d) for systems composed of D20A20-diblock copolymers (black) or A10D20A10-triblock copolymers (orange) as a function of the Flory-Huggins interaction parameter.

ADA-triblock copolymers as a function of the χ-parameter, obtained with the DMC-SCFT method. We compare these results to the respective equilibrium morphologies for the diblock-copolymer as well as triblock-copolymer systems, shown in Figs. 2(a) and 2(b), respectively. From this analysis, we infer that the EDE of the triblock-copolymer system is always higher compared to the diblock-copolymer system over the whole range of χ-parameters and that this difference in efficiency vanishes in the limit of high χ-parameters. Moreover, we note that in case of the triblock-copolymer system the EDE curve decreases nearly steadily with increasing χ-parameter, whereas in case of the diblock-copolymer system it reaches a minimum for the morphology V at a χ-value of 0.5 and, then, increases slowly for higher χ-values. To understand the causes for the reduction in the EDE and the corresponding charge losses, we consider next in Fig. 3(c) the length of the DA-interface for both block-copolymer systems as a function of the Flory-Huggins parameter. We deduce from the graph that the interfacial length of the triblock-copolymer system is always larger in magnitude compared to the one of the diblock-copolymer system over the whole range of χ-parameters. Moreover, we note that the difference in the quantity between both block-copolymer types decreases rapidly up to a χ-value of 0.4 and afterwards decreases only slowly for larger χ-values. This shows that the large difference in the EDE between the triblock- and diblock-copolymer systems at low χ-parameters is partly due to the difference in size of the DA interface, allowing a higher exciton dissociation in the former case. Next, we consider in Figs. 4 and 5, respectively, the charge density and exciton dissocia-

tion frequency for both block-copolymer systems as a function of the Flory-Huggins interaction parameter. In the case of the diblock-copolymer system, we see that the morphologies II−V possess large regions of negative or positive charge accumulations and that these regions are characterized by a low exciton dissociation frequency, causing substantial charge losses. We further note that the most important contributions to the charge accumulation in this regime are provided by dead-end- and bottleneck-type of defects. We conclude from these observations that, in addition to the decrease of the interfacial length, charge accumulation in defects counteracts charge generation and, thus, provides an additional contribution to the loss of charges in the case of these morphologies. As a consequence, the EDE is decreasing to a minimum in this regime. With increasing χ-parameter, these regions of accumulated charges vanish successively, which results in a smooth increase of the EDE as shown in Fig. 3(a). Similar observations can be made for the triblock-copolymer system. In this case, we find that the largest drops in the EDE, observed in the ranges $\chi = 0.3-0.4$ and $\chi = 0.6-0.9$, correlate with the morphologies with the largest charge accumulations, i.e., morphologies (III and IV) for the first drop and morphologies (VI−IX) for the second drop. In conclusion, we see that both the decrease of the interfacial length as well as a high charge accumulation are the primary factors for the deterioration of the EDE. Both effects can lead to an effective charge carrier loss and, thus, to a reduced IQE. Let us next compare the CTE curves of the diblock- and triblock-copolymer system, visualized in Figs. 3(a) and 3(b), respectively. From the plots, we deduce that the CTE curve of the diblock-copolymer
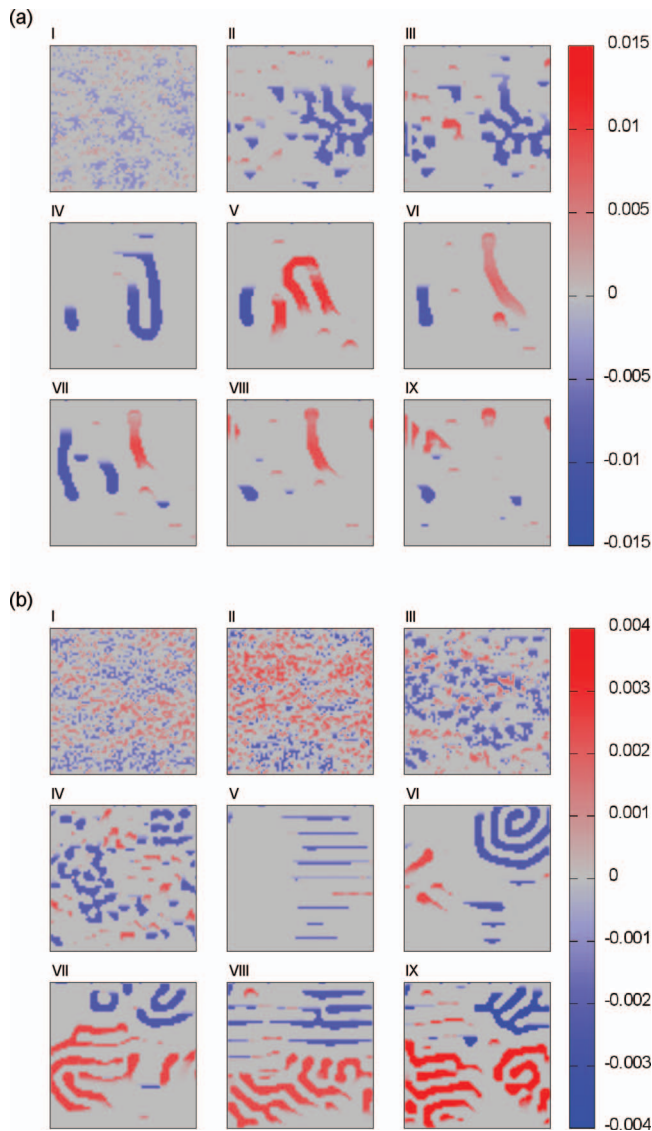
FIG. 4. Charge density for a system composed of (a) D20A20-diblock copolymers or (b) A10D20A10-triblock copolymers as a function of the Flory-Huggins interaction parameter, obtained with the DMC-SCFT method. Electrodes are applied in horizontal direction for all morphologies [blue: negative charge (electron); red: positive charge (hole)].
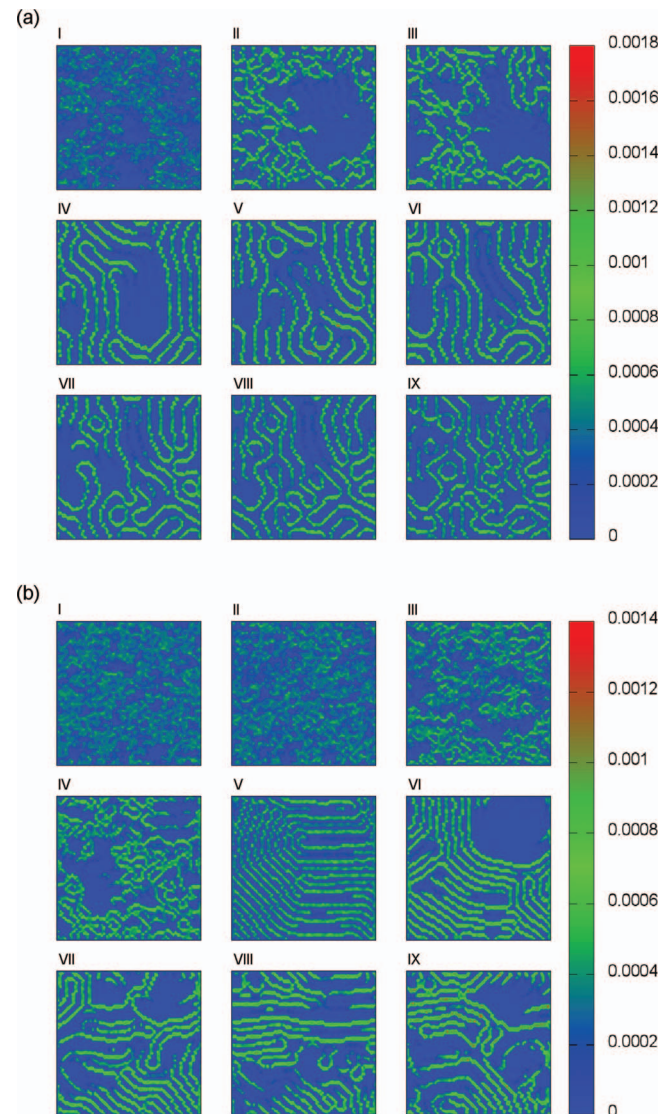

FIG. 5. Frequency of exciton dissociation for a system composed of (a) D20A20-diblock or (b) A10D20A10-triblock copolymers as a function of the Flory-Huggins interaction parameter, obtained with the DMC-SCFT method.

system increases steeply from low χ-values up to a maximum of 74% at $\chi = 0.4$ and, then, stabilizes by oscillating around a high CTE value of 50% at larger χ-values. For the triblock-copolymer system, instead, the CTE curve passes through a distinct maximum of 40% at $\chi = 0.6$ and subsequently drops to a CTE of around 10% at higher χ-values. To better understand the causes for these maxima in the CTE, we consider in Fig. 3(d) the total numbers of recombinations for both block-copolymer types as a function of the χ-parameter. By comparing these latter curves to the CTE curves in Figs. 3(a) and 3(b), we conclude that the maxima in the CTE correlate with minima in the total number of recombinations in both cases. Moreover, by further analyzing the two quantities for the triblock-copolymer system in the regime of large χ-values, we see that the morphology IX at $\chi = 0.9$ corresponds to a second minimum in the number of recombinations of similar magnitude as in case of morphology VI at

$\chi = 0.6$, which however in this case results in a low CTE of only 15%. This shows that the CTE is not only affected by charge losses due to charge recombinations. To find additional charge-loss effects influencing the CTE, we analyze in Fig. 4 the charge-density distributions for the triblock-copolymer system of the two morphologies previously mentioned. We observe that for morphology IX strong accumulations of negative and positive charges take place in the various bottlenecks as well as dead ends throughout the whole nanostructure, whereas for the morphology VI negative charges accumulate only in a spiral-like defect in the upper-right corner of the charge-density plot. We conclude from these findings that these defect types act as permanent charge traps, leading, beside the charge recombinations, to additional charge losses and consequently to a further deterioration of the CTE. Moreover, we observe that charge-carrier trapping is promoted in dead-end-like nanostructures, where charges of opposite sign are captured nearby and attract each other through internal electrical fields, ultimately providing regions of strong charge

accumulations as in case of the triblock-copolymer morphologies (VII−IX). To elucidate the prerequisites favoring one or the other charge-loss mechanism, we study in the following the physical characteristics leading to charge trapping or charge recombination. Common to both cases is that one type of charge carriers is slowed down or even fully hindered to reach the electrode by a bottleneck or dead end at the level of the mesoscale morphology, resulting in a local increase of the concentration of this charge carrier type at this specific location. Moreover, in case of the charge-trapping mechanism fast removal of charges of opposite sign in the adjacent phases and subsequent extraction at the respective electrode cause a lack of charges in this region of the defect, which disfavors the process of charge recombination with regard to the charge accumulation process. These phases are generally characterized by direct percolation paths to one of the electrodes, allowing fast extraction of charges with opposite sign. By contrast, in case of the charge-recombination mechanism fast supply of opposite charges in adjacent phases causes a considerable number of charge recombinations, counteracting the process of charge accumulation. As can be inferred from the charge-recombination number distributions of the diblock-copolymer system in Fig. 6(a), this loss mechanism occurs particularly frequently in case of the morphologies (I−III), where the low degree of phase separation and fine dispersion of D- and A-phases throughout the system, leads to high availability of charges for geminate charge recombination and, thus, to a broad distribution of recombination events throughout the system. Moreover, in case of morphology IV, which has the lowest total number of recombinations, we observe only a few localized sites with a high number of recombinations, which concentrate around the small number of bottlenecks. With increasing χ-parameter (morphologies: IV−IX), the total number of defects increases in the system, leading to a larger number of sites with high recombination number. Similar observations can be made in case of the triblock-copolymer system in Fig. 6(b), which is characterized by a homogeneous distribution of charge-recombination events at low χ-parameter giving rise to a high total number of recombinations (morphologies: I−IV). With increasing χ-parameter, the degree of phase separation increases and the recombination events become more localized around the defects, resulting in high recombination numbers at these sites. Finally, by comparing Figs. 2(a) and 2(b) to Figs. 3(a) and 3(b), we conclude that in the case of both block-copolymer systems the morphologies with the largest number of continuous percolation paths and the highest degree of phase separation possess the highest CTE, i.e., morphology IV for the diblock-copolymer system and morphology VI for the triblock-copolymer system.

To evaluate the overall photovoltaic performance of solar cells based on diblock- and triblock-copolymers, we consider next in Figs. 3(a) and 3(b), their IQEs as a function of the Flory-Huggins interaction parameter and analyze them with regard to the morphological characteristics, visualized in Fig. 2. We see that the IQE curves of both block-copolymer systems essentially possess the same functional behavior as the corresponding CTE curves, however leveled down in magnitude by their respective EDEs. Moreover, by
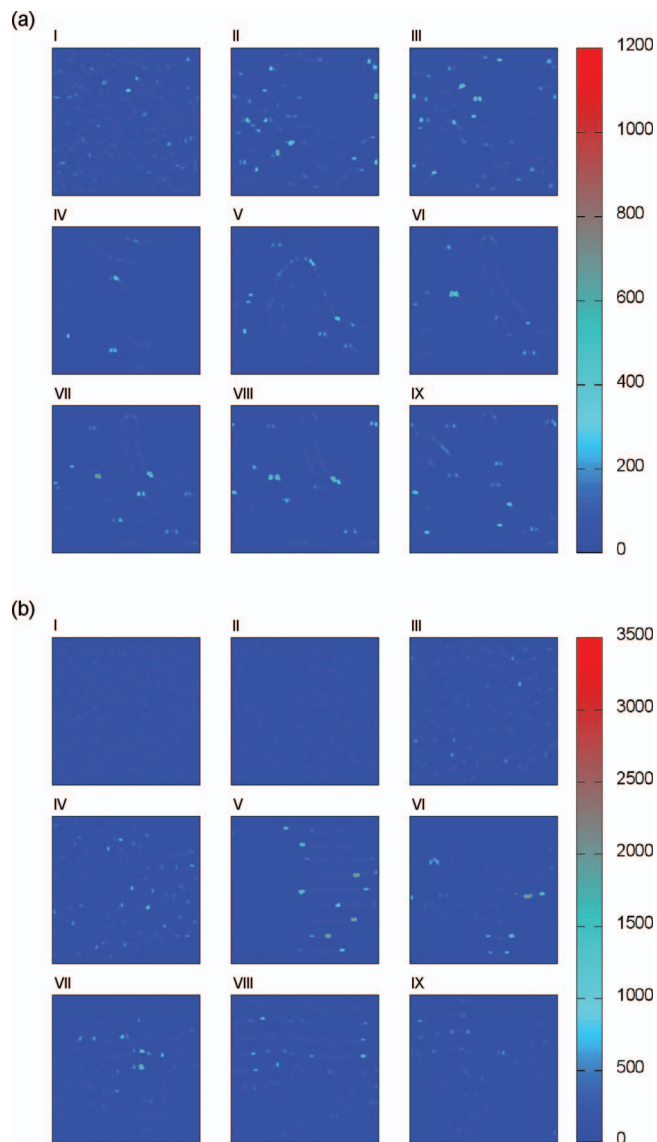

FIG. 6. Charge-recombination number distribution for a system composed of (a) D20A20-diblock or (b) A10D20A10-triblock copolymers as a function of Flory-Huggins interaction parameter, obtained with the DMC-SCFT method.

comparing the IQE curves of both polymer systems, we deduce that the diblock-copolymer system has a slightly higher IQE than the triblock-copolymer system over the whole range of χ-parameters. This essentially relates to its larger CTE, which is not compensated by the higher EDE in the triblock-copolymer case. Next, we analyze the impact of mechanical stress on the photovoltaic performance of triblock-copolymer systems, which are known to form stable networks of physical crosslinks conferring those materials useful properties for flexible nanodevice applications. To this end, we show in Fig. 7 the IQE, EDE, and CTE for morphology VI of the triblock-copolymer system discussed previously as a function of the mechanical load at different moduli of the D- and A-phases. It is worth noting in this regard that, because we used the theory of linear elasticity in conjunction with the finite-element method, the mechanical loads applied here pertain to the linear regime of mechanical properties.[30,52] As can be deduced from Fig. 7(a), the IQE curves of all block-copolymer
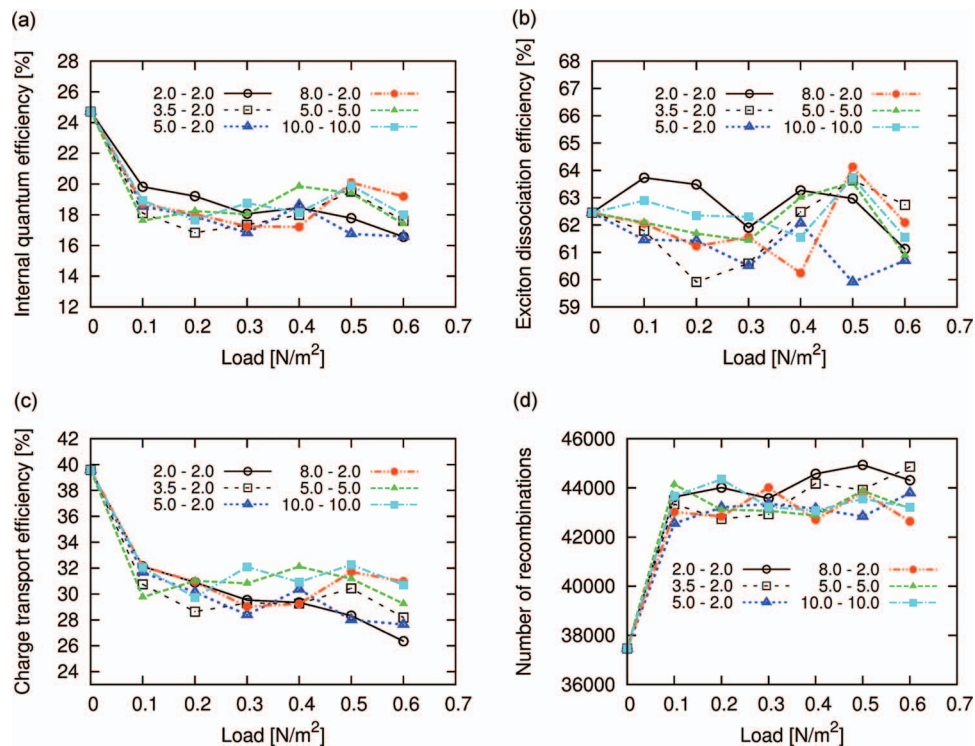
FIG. 7. (a) Internal quantum efficiency, (b) exciton dissociation efficiency, (c) charge transport efficiency as well as (d) total number of recombinations for a system composed of A10D20A10-triblock copolymers as a function of the external mechanical load at different bulk moduli for the D- and A-phases, obtained with the DMC-SCFT method. Note that the mechanical loads were applied on the morphology VI of the triblock-copolymer system, which is the morphology with the highest internal quantum efficiency.

systems decrease moderately at small mechanical loads and afterwards they stabilize by performing small- up to medium-sized oscillatory changes at higher loads, whose magnitudes strongly depend on the moduli of the different phases. We point out in this context that our findings are confirmed by the recent mechanical measurements of Kaltenbrunner *et al.*[53] on ultrathin bulk heterojunction polymer solar cells composed of poly(3-hexylthiophene) (P3HT) and (6,6)-phenyl-C61-butyric-acid-methyl ester (PCBM). These authors found through cyclic compression and stretching of their samples to 50% a gradual decrease in power up to 27% after 22 cycles, leading to a successive degradation of the photovoltaic performance of the material. Moreover, by further comparing Fig. 7(a) with the corresponding EDE and CTE curves in Figs. 7(b) and 7(c), we conclude that the CTE possesses a similar functional behavior than the IQE, whereas the EDE exhibits only moderate deviations from the starting value of 62.5% over the whole range of mechanical loads. This demonstrates that in this range of parameters the dependence of the IQE on the mechanical changes is mainly influenced by the CTE; however, it is only marginally affected by the EDE. To analyze in more detail the causes for the deterioration of the CTE with increasing mechanical load, we show in Fig. 7(d) the total number of recombinations as a function of the externally applied mechanical load. We observe that up to a mechanical load of 0.1 N/m^2 the quantity strongly increases for all systems with different moduli for the D- and A-phases, which demonstrates that in this regime the reduction in the IQE is primarily caused by loss processes due to charge recombination. Moreover, we note that with increasing

mechanical load the quantity reaches a plateau, which correlates with the reduced supply of opposite charges enabling charge recombination in proximity of the bottleneck- or dead-end type of defects. The effectiveness and type of loss mechanism experienced by the charges in a defect are strongly determined by the local deformation of the nanophases. These findings are confirmed by considering the volume fractions of the strained morphologies at mechanical loads of 0.1 N/m^2 and 0.5 N/m^2 in Figs. 1S and 2S (see the supplementary material) in conjunction with the corresponding charge density distributions as well as frequencies of exciton dissociation in Figs. 3S−6S (see the supplementary material), respectively.[54] Moreover, from Figs. 7(c) and 7(d) we infer that at a load of 0.5 N/m^2 the CTE curves of the morphologies with $K_A =$ 5.0 GPa, $K_D = 2.0$ GPa, and $K_A = 2.0$ GPa, $K_D = 2.0$ GPa possess almost the same values, despite a strongly differing charge recombination number. This indicates that, under these conditions, a large number of charges are lost due to a loss process other than the charge-recombination process. To further elucidate this issue, we consider next the charge-density distributions of the corresponding strained morphologies in Fig. 4S (see the supplementary material). From the charge-density distribution of the strained morphology III, we deduce that in the upper left part of the plot there is a region of strong negative charge accumulation, which is not observed in the other cases. As can be deduced from Fig. 2S (see the supplementary material), this region is part of the spiral-like defect, which acts as a dead end for the electrons and hinders in this way their migration to the respective electrode. Due to the lack of opposite charges in this part of the system, charge
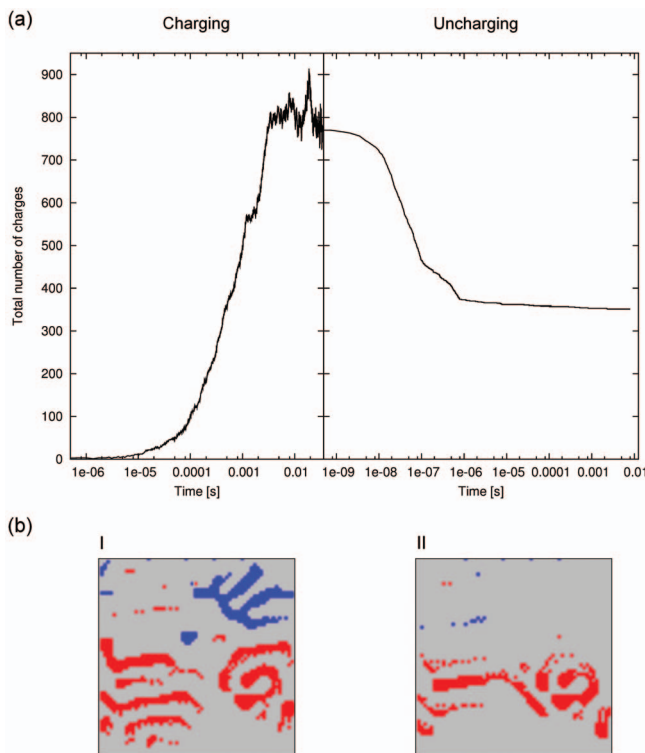
FIG. 8. (a) Total number of charges during charging- or uncharging-process as a function of time and (b) charge density distributions after (I) charging- or (II) uncharging-process for morphology IX of a system composed of A10D20A10-triblock copolymers, obtained with the DMC-SCFT method. Electrodes for this morphology were applied in horizontal direction.

losses due to charge recombinations become less probable, whereas charge losses due to charge trapping, going along with a deterioration of the exciton dissociation, are favored. The latter conclusion can be drawn from Fig. 6S (see the supplementary material), where a reduction of the exciton dissociation frequency is observed in the region of negative charge accumulation mentioned previously. As a consequence, these additional loss processes cause that the strained morphology III possesses the lowest EDE, CTE, and IQE of all morphologies at a load of 0.5 N/m^2, whereas their effective suppression in case of morphology IV with $K_A = 8.0$ GPa, $K_D = 2.0$ GPa leads to the highest efficiencies at the same load.

In the previous analysis, we have found that in some of the nanostructured morphologies a significant amount of charges is accumulated, such as in the case of the triblock-copolymer morphologies (VII−IX). By assuming that these charges could be stored for a certain period of time and afterwards regained through a change of the environmental conditions, we conjecture that these systems could be used for the purpose of charge storage. To investigate this aspect in more detail, we show in Fig. 8(a) the total number of charges as a function of the charging or uncharging time during the process of charge loading or charge unloading of the morphology IX. The charging of the system is accomplished by carrying out the photovoltaic process, whereas uncharging is achieved by reversing the polarity of the net electric field after the charging process has been completed. We deduce from the graph that during the charging process the total number of charges increases significantly up to a simulation time of

0.0025 s and, then, reaches a plateau with a maximum amount of 800 charges up to the end of the charging process, which corresponds to a stationary solution of the DMC algorithm. In the case of the uncharging process, by contrast, we see that the total number of charges possesses a regime of fast decrease up to a simulation time of 10^{-7} s, which is followed by a regime of slow decay in the timerange from 10^{-7} s up to 10^{-6} s. In the final stage, the curve attains a plateau with a total number of 350 charges, which relates to the fact that some of the charges remain trapped in the defects and, thus, cannot be extracted from the device. This can be inferred from Fig. 8(b), where we show the charge density distributions of morphology IX, obtained after the (I) charging- and (II) uncharging-process, respectively. By comparing both figures to the volume fractions of the morphology IX in Fig. 2(b), we deduce that the major part of the accumulated electrons and holes could be extracted from regions with direct percolation paths to the electrodes, whereas in regions with bottleneck- or dead-end-type of defects a smaller fraction of holes remained captured and, thus, was hindered to reach the respective electrode. This finding is further confirmed through the simulation movie of the uncharging process, which is provided in the supplementary material of this paper.[54] Finally, we emphasize that these trapped charges can only decay through the process of charge recombination and, thus, cause a decrease of the charge storage efficiency of the device.

IV. SUMMARY AND OUTLOOK

In summary, in this work we have presented a multiscale study, in which we explored the causes affecting the photovoltaic performance of nanophase-separated polymer-based solar cell materials with changing inter-monomeric interaction strength, chain architecture and mechanical loads, applied on the system. To this end, we made use of the DMC-SCFT algorithm, which combines the self-consistent field theory method, to generate the equilibrium nanostructured morphologies, with a dynamic Monte Carlo algorithm, to model the elementary photovoltaic processes. For the investigations, we considered block-copolymer systems, which provide long-time stable thin-film nanostructured morphologies with optimal physical properties for flexible applications. From our calculation results, we deduced that in the range from low up to intermediate χ-parameters an increasing number of continuous percolation paths are formed with growing interaction strength between the monomers. In this parameter range, the CTE and IQE increase up to a maximum, characterized by a minimum in the number of charge losses due to charge recombination. In the regime of high χ-parameters both block-copolymer systems form nanostructures with a large number of bottlenecks and dead ends, leading to a large number of charge losses due to charge recombination, charge trapping, and a deterioration in exciton dissociation. These loss mechanisms lead to a significant drop in the CTE and IQE for both types of block-copolymer systems in this parameter range. Moreover, by comparing the IQE curves of both polymer systems, we deduce that the diblock-copolymer system possesses a slightly higher IQE than the triblock-copolymer system over the whole range of χ-parameters.

This essentially relates to its larger CTE, which is not compensated by the higher EDE in the triblock-copolymer case. By further subjecting the triblock-copolymer morphology with the highest IQE to different mechanical loads, we find that the photovoltaic performance of the material decreases with increasing external mechanical stress, caused by a growing number of charge losses due to charge recombination and charge accumulation. Finally, we have also demonstrated on the example of a system of triblock copolymers that the process of charge trapping in defects can be reversed by changing the polarity of the electrodes, which might confer these materials the ability to be used as charge storage media.

ACKNOWLEDGMENTS

[1]G. Li, R. Zhu, and Y. Yang, Nature Photon. **6**, 153 (2012).

[2]A. C. Arias, J. D. MacKenzie, I. McCulloch, J. Rivnay, and A. Salleo, Chem. Rev. **110**, 3 (2010).

[3]Y. Sun, S.-C. Chien, H.-L. Yip, K.-S. Chen, Y. Zhang, J. A. Davies, F.-C. Chen, B. Lin, and A. K.-Y. Jen, J. Mater. Chem. **22**, 5587 (2012).

[4]S.-S. Sun, C. Zhang, A. Ledbetter, S. Choi, K. Seo, and J. Haliburton, Appl. Phys. Lett. **90**, 043117 (2007).

[5]A. Pershin, S. Donets, and S. A. Baeurle, J. Chem. Phys. **136**, 194102 (2012).

[6]S. Sun, Z. Fan, Y. Wang, and J. Haliburton, J. Mater. Sci. **40**, 1429 (2005).

[7]G. L. C. Paulus, S. Shimizu, J. T. Abrahamson, J. Zhang, A. J. Hilmer, and M. S. Strano, AIChE J. **57**, 1104 (2011).

[8]O. V. Mikhnenko, F. Cordella, A. B. Sieval, J. C. Hummelen, P. W. M. Blom, and M. A. Loi, J. Phys. Chem. B **112**, 11601 (2008).

[9]F. Cordella, R. Orru, M. A. Loi, A. Mura, and G. Bongiovanni, Phys. Rev. B **68**, 113203 (2003).

[10]I. B. Martini, A. D. Smith, and B. J. Schwartz, Phys. Rev. B **69**, 035204 (2004).

[11]A. J. Lewis, A. Ruseckas, O. P. M. Gaudin, G. R. Webster, P. L. Burn, and I. D. W. Samuel, Org. Electron. **7**, 452 (2006).

[12]S. R. Cowan, N. Banerji, W. L. Leong, and A. J. Heeger, Adv. Funct. Mater. **22**, 1116 (2012).

[13]A. Pivrikas, G. Juska, A. J. Mozer, M. Scharber, K. Arlauskas, N. S. Sariciftci, H. Stubb, and R. Osterbacka, Phys. Rev. Lett. **94**, 176806 (2005).

[14]S. R. Cowan, W. L. Leong, N. Banerji, G. Dennler, and A. J. Heeger, Adv. Funct. Mater. **21**, 3083 (2011).

[15]S. R. Cowan, A. Roy, and A. J. Heeger, Phys. Rev. B **82**, 245207 (2010).

[16]W. L. Leong, S. R. Cowan, and A. J. Heeger, Adv. Energy Mater. **1**, 517 (2011).

[17]C. G. Shuttle, B. O'Regan, A. M. Ballantyne, J. Nelson, D. D. C. Bradley, J. de Mello, and J. R. Durrant, Appl. Phys. Lett. **92**, 093311 (2008).

[18]O. G. Reid, G. E. Rayermann, D. C. Coffey, and D. S. Ginger, J. Phys. Chem. C **114**, 20672 (2010).

[19]S.-S. Sun, Z. Fan, Y. Wang, K. Winston, and C. E. Bonner, Mater. Sci. Eng. B **116**, 279 (2005).

[20]M. D. McGehee and M. A. Topinka, Nature Mater. **5**, 675 (2006).

[21]S. M. Lindner, S. Hüttner, A. Chiche, M. Thelakkat, and G. Krausch, Angew. Chem., Int. Ed. **45**, 3364 (2006).

[22]S. A. Baeurle, J. Math. Chem. **46**, 363 (2009).

[23]E. Peter, B. Dick, and S. A. Baeurle, J. Chem. Phys. **136**, 124112 (2012).

[24]M. Karplus and J. Kuriyan, Proc. Natl. Acad. Sci. U.S.A. **102**, 6679 (2005), and references therein.

[25]D. Frenkel and B. Smit, *Understanding Molecular Simulation: From Algorithms to Applications* (Academic, San Diego, 2003).

[26]G. Santangelo, A. Di Matteo, F. Müller-Plathe, and G. Milano, J. Phys. Chem. B **111**, 2765 (2007).

[27]P. Carbone, H. A. Karimi-Varzaneh, and F. Müller-Plathe, Faraday Discuss. **144**, 25 (2010).

[28]W. L. Jorgensen, D. S. Maxwell, and J. Tirado-Rives, J. Am. Chem. Soc. **118**, 11225 (1996).

[29]V. Rühle, C. Junghans, A. Lukyanov, K. Kremer, and D. Andrienko, J. Chem. Theory Comput. **5**, 3211 (2009).

[30]S. A. Baeurle, G. H. Fredrickson, and A. A. Gusev, Macromolecules **37**, 5784 (2004).

[31]S. A. Baeurle, Phys. Rev. Lett. **89**, 080602 (2002).

[32]F. Schmid, "Theory and simulation of multiphase polymer systems," in *Handbook of Multiphase Polymer Systems*, edited by A. Boudenne, L. Ibos, Y. Candau, and S. Thomas (Wiley, Chichester, 2011), Chap. 3.

[33]G. H. Fredrickson, *The Equilibrium Theory of Inhomogeneous Polymers* (Clarendon, Oxford, 2006).

[34]S. A. Baeurle, M. G. Kiselev, E. S. Makarova, and E. A. Nogovitsin, Polymer **50**, 1805 (2009).

[35]K. C. Daoulas and M. Müller, J. Chem. Phys. **125**, 184904 (2006).

[36]D. Düchs, V. Ganesan, G. H. Fredrickson, and F. Schmid, Macromolecules **36**, 9237 (2003).

[37]E. Helfand, J. Chem. Phys. **62**, 999 (1975).

[38]F. Schmid, J. Phys.: Condens. Matter **10**, 8105 (1998).

[39]T. Honda and T. Kawakatsu, Macromolecules **39**, 2340 (2006).

[40]T. Kawakatsu, *OCTA Integrated Simulation System for Soft Materials*, User's manual, Version 8.0 (2009), Chap. 7, p. 134.

[41]M. Doi, Macromol. Symp. **195**, 101 (2003).

[42]See http://octa.jp/ for information about OCTA program.

[43]D. T. Gillespie, Annu. Rev. Phys. Chem. **58**, 35 (2007).

[44]L. Meng, Y. Shang, Q. Li, Y. Li, X. Zhan, Z. Shuai, R. G. E. Kimber, and A. B. Walker, J. Phys. Chem. B **114**, 36 (2010).

[45]X. Zhan, Z. Tan, B. Domercq, Z. An, X. Zhang, S. Barlow, Y. Li, D. Zhu, B. Kippelen, and S. R. J. Marder, J. Am. Chem. Soc. **129**, 7246 (2007).

[46]R. A. Marsh, C. Groves, and N. C. Greenham, J. Appl. Phys. **101**, 083509 (2007).

[47]R. A. Marcus, Rev. Mod. Phys. **65**, 599 (1993).

[48]K. Seki and M. Tachiya, Phys. Rev. B **65**, 014305 (2001).

[49]R. G. E. Kimber, A. B. Walker, G. E. Schröder-Turk, and D. J. Cleaver, Phys. Chem. Chem. Phys. **12**, 844 (2010).

[50]P. K. Watkins, A. B. Walker, and G. L. B. Verschoor, Nano Lett. **5**, 1814 (2005).

[51]M. Casalegno, G. Raos, and R. Po, J. Chem. Phys. **132**, 094705 (2010).

[52]See http://octa.jp/OCTA/presen/muffin_eng.pdf for information about software tool muffin/elastica within the octa program.

[53]M. Kaltenbrunner, M. S. White, E. D. Glowacki, T. Sekitani, T. Someya, N. S. Sariciftci, and S. Bauer, Nat. Commun. **3**, 770 (2012).

[54]See supplementary material at http://dx.doi.org/10.1063/1.4792366 for the volume fractions, charge density distributions as well as frequencies of exciton dissociation of the strained ADA-triblock copolymer morphologies at mechanical loads of 0.1 N/m^2 and 0.5 N/m^2 and for movie about charge storage device.